Biochar X https://doi.org/10.48130/bchax-0026-0019

Original Research Open Access

Tailoring the porosity and surface chemistry of *Sargassum* biochar for enhanced CO_2 capture

Yuanling Li[1,2], Tao Wang[2,3], Jinyu Zhu[1], Siyu Duan[1] and Lina Liu[2*]

Received: 16 April 2026
Revised: 4 June 2026
Accepted: 15 June 2026
Published online: 27 July 2026

Abstract

In this study, a highly efficient, sustainable, and low-cost solid CO_2 adsorbent was developed using algal bloom waste from *Sargassum*, achieving the dual goals of carbon capture and waste valorization. To overcome the limitations of a low specific surface area and the unfavorable surface chemistry of *Sargassum*-derived biochar, the study investigated the effects of pyrolysis temperature (400, 500, 600, and 700 °C) and KOH modification on the biochar's properties and CO_2 capture performance. The biochar was characterized in detail to determine its physicochemical properties and CO_2 capture capacities. The results demonstrated that the highest CO_2 capture capacity (120.5 mg/g, 313 K) was achieved by the sample modified with KOH prior to pyrolysis at 400 °C (Sar-KOH), which retained 98.9% of its initial capacity after nine regeneration cycles. The high performance is attributed to a synergistic effect: KOH activation created a developed microporous structure conducive to physisorption, while the moderate pyrolysis temperature preserved a high density of surface hydroxyl groups, enhancing adsorption via hydrogen bonding with CO_2 molecules. This study elucidates the critical roles of the pyrolysis temperature and KOH activation sequence in tailoring the pore structure and surface chemistry of algal biochar, paving the way for the rational design of high-performance adsorbents for CO_2 capture applications.

Keywords: Carbon capture, Biochar, Pyrolysis temperature, Hydroxyl group, Adsorption mechanism

Highlights

- The porous *Sargassum* biochar Sar-KOH exhibits a high CO_2 capture capacity.
- Sar-KOH possesses the highest abundance of micropores and hydroxyl groups.
- The developed micropore structure facilitates the physisorption of CO_2.
- The hydroxyl groups enhance adsorption by interacting with CO_2.

* Correspondence: Lina Liu (liuln@nankai.edu.cn)
Full list of author information is available at the end of the article.

https://doi.org/10.48130/bchax-0026-0019

Graphical abstract

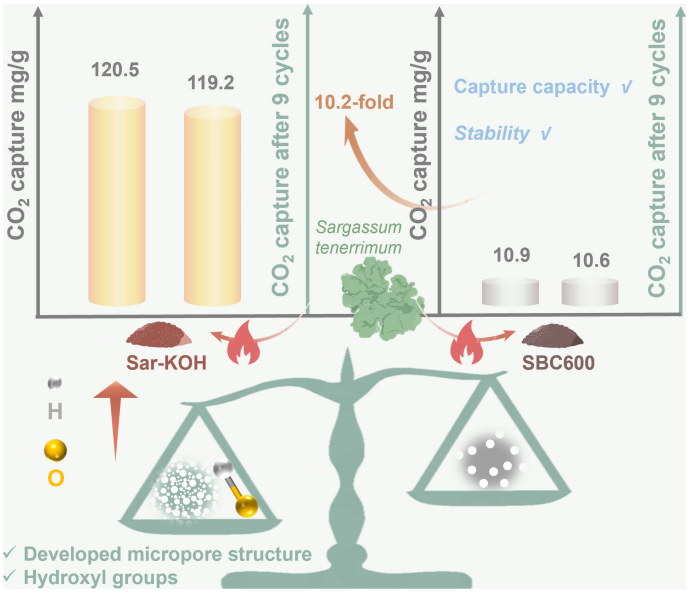

Introduction

The Intergovernmental Panel on Climate Change (IPCC) underscores that limiting the increase in global average temperature to less than 1.5 °C above preindustrial levels is crucial to preventing a climate catastrophe[1]. Aligned with this goal, the Paris Agreement has set a target of achieving net zero CO_2 emissions by 2050[2]. However, the persistent and dominant reliance on fossil fuels continues to drive excessive CO_2 emissions, presenting a major challenge to these climate objectives[3,4]. Therefore, investigation of decarbonizing existing industrial processes is ongoing; however, for hard-to-abate sectors, CO_2 capture remains essential to achieving net zero targets.

In recent years, solid adsorbents for CO_2 capture, including zeolites, boron nitride[5,6], porous organic polymers[7], MXene-based materials[8], metal–organic frameworks[9], covalent organic frameworks[10], and porous carbon materials[11], have attracted increasing attention because of their high efficiency, favorable kinetics, and relatively low regeneration energy. Among them, porous biochar, a solid product derived from the thermochemical conversion of biomass[12–15], has emerged as a promising candidate because of its low cost, environmental friendliness with net negative greenhouse gas emissions during production (around −0.9 kg CO_2 equivalent per kg), high specific surface area, and abundant surface functional groups[16,17]. Although current research has largely focused on terrestrial biomass wastes (e.g., agricultural residues, sewage sludge, livestock manure)[13,18–21], their use competes directly with the bioenergy industry for the same renewable feedstocks. Marine biomass wastes, particularly algae and seaweed residues, offer a promising alternative because of their high abundance, superior productivity, and minimal competition with arable land[22]. Moreover, the increasing frequency of harmful macroalgal blooms worldwide generates vast amounts of biomass that could be valorized into high-value products, addressing both environmental and resource challenges[23,24].

Despite this potential, algae-derived biochars (ABCs) exhibit lower CO_2 adsorption capacity and selectivity compared with advanced porous carbon materials. This performance gap necessitates the development of strategies to precisely tailor the pore structure and surface chemistry of ABCs, which are critical for enhanced CO_2 adsorption performance. Chemical activation, particularly with agents like KOH and NaOH, is recognized as an effective approach to address both the pore structure and surface chemistry simultaneously[25]. The activation mechanism in KOH-modified biochar involves etching the carbon matrix with potassium-containing species (e.g., K_2O, K_2CO_3) formed during pyrolysis[26]. This process not only widens the existing pores but also creates new pores, significantly developing the porosity. Crucially, such ultramicropores (pores narrower than ~0.7 nm) are identified as the most effective for physisorption of CO_2 at ambient conditions, which is caused by the enhanced adsorption potential within these confined spaces[27]. In parallel with chemical modification, pyrolysis temperature is also a key factor for controlling biochar's properties. Higher pyrolysis temperatures generally promote more complete devolatilization and carbonization, which can open blocked pore channels and increase the specific surface area and pore volume, favoring physisorption capacity[28]. However, this often comes at the cost of thermal decomposition of heteroatom-containing functional groups (e.g., –OH, $–NH_2$), which are vital for surface interactions with CO_2. This complex trade-off necessitates exploring a synergistic strategy that optimally combines thermal treatment with chemical modification to achieve high performance. Therefore, to investigate the individual and synergistic effects of the pyrolysis temperature and KOH modification sequence on the physicochemical properties and CO_2 adsorption performance of ABCs, biochar derived from *Sargassum tenerrimum* (SBC) was selected as a representative model of marine macroalgal biomass because of its typical harmful bloom-forming nature and intrinsically low specific surface area that poses a challenging test for activation strategies.

We hypothesize that the sequence of KOH activation relative to the pyrolysis temperature can synergistically regulate the microporous structure and surface functional groups of SBCs, thereby overcoming their intrinsic limitations (low specific surface area and unfavorable surface chemistry) to achieve enhanced CO_2 capture performance. The novelty of this work lies in (i) disentangling the effects of the pyrolysis temperature (400–700 °C) and KOH modification sequence on the physicochemical properties of SBCs; (ii) revealing

that a moderate pyrolysis temperature (400 °C) combined with prepyrolysis KOH activation preserves abundant surface hydroxyl groups while developing microporosity; and (iii) demonstrating that this synergistic strategy yields a CO_2 capture capacity comparable to or exceeding that of many synthetic porous materials, using a harmful algal bloom waste as feedstock. This temperature range was selected according to the thermal degradation behavior of *Sargassum* biomass: Below 400 °C, carbonization is incomplete with poorly developed porosity, whereas above 700 °C, the oxygen-containing functional groups are almost completely eliminated, thereby transitioning from a surface-chemistry-dominated adsorption regime to a porosity-dominated regime. Therefore, a series of SBCs were prepared at different pyrolysis temperatures (400, 500, 600, and 700 °C). For the sample pyrolyzed at 400 °C, both prepyrolysis and postpyrolysis KOH activation strategies were applied. The choice of a moderate pyrolysis temperature of 400 °C was motivated by two reasons. First, higher pyrolysis temperatures would decompose oxygen-containing functional groups (e.g., –OH, –COOH), which facilitate the chemisorption of CO_2 through hydrogen bonding. To achieve a synergistic effect between physical and chemical adsorption, a moderate temperature is necessary to preserve these functional groups. Second, even at this moderate temperature, KOH remains capable of reacting with the carbon precursor to generate microporosity[29,30]. Therefore, 400 °C was selected as the optimal temperature to balance porosity development and surface chemistry.

In the present study, we demonstrated that the pyrolysis temperature and KOH premodification are critical parameters for optimization of the porous structure and chemical properties of SBC. The synergistic effect of KOH activation and a moderate pyrolysis temperature (400 °C) optimally facilitates the formation of abundant micropores and surface hydroxyl groups. This dual enhancement of adsorption sites is key to achieving high CO_2 capture capacity.

Experimental section

Materials

The *S. tenerrimum* used in this study was purchased from a farm located in Wenzhou city (Zhejiang, China). KOH (> 99% purity) was obtained from Shanghai Macklin Biochemical Technology Co., Ltd. (Shanghai, China). Hydrochloric acid (HCl, >37% purity) was purchased from Tianjin Sheng'ao Chemical Reagents Co., Ltd (Tianjin, China). The CO_2 adsorption experiments were conducted using CO_2 (purity > 99.999%) and N_2 (purity > 99.999%), purchased from Tianjin Baishida Gas Co., Ltd (Tianjin, China). The resulting biochars were washed with 3 M HCl to remove inorganic impurities and rinsed with deionized (DI) water until reaching a neutral pH. DI water was used for the experiment.

Preparation of SBC

The entire preparation process of biochar is shown in Fig. 1. Specifically, the *S. tenerrimum* was washed with DI water repeatedly to remove impurities, and then dried overnight in an oven at 80 °C. The dried *S. tenerrimum* was ground into powder and collected via sifting through an 80-mesh sieve. The collected *S. tenerrimum* powder was pyrolyzed from 50 °C to the target temperatures of 400–700 °C at a rate of 10 °C/min under an N_2 atmosphere and held at the target temperature for 120 min. The resulting biochars are denoted as SBC400, SBC500, SBC600, and SBC700, according to the pyrolysis temperature.

Preparation of Sar-KOH and SBC400-KOH

Sar-KOH: For a typical synthesis procedure, 2.0 g of dried *S. tenerrimum* powder and 2.0 g of KOH were dispersed into 60 mL of DI water. The mixture was stirred at 500 rpm for 12 h and then dried overnight in an oven at 80 °C. The dried sample (denoted Sar-KOH) was then pyrolyzed from 50 to 400 °C with a heating rate of 10 °C/min for 2 h under an N_2 atmosphere.

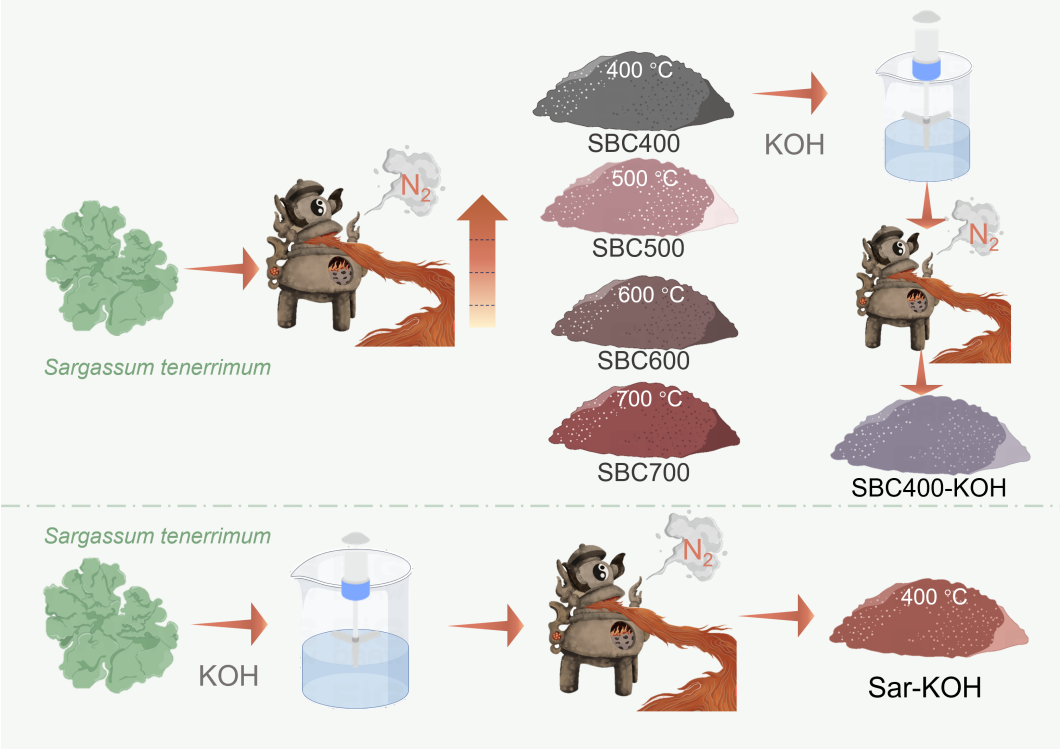

Fig. 1 Schematic diagram of the preparation of biochars from *Sargassum tenerrimum*.

SBC-400-KOH: To produce the sample, 2.0 g of SBC400 powder and 2.0 g of KOH were dispersed into 60 mL of DI water. The mixture was stirred at 500 rpm for 12 h and dried overnight in an oven at 80 °C. The dried sample (denoted SBC400-KOH) was then pyrolyzed from 50 to 400 °C at a heating rate of 10 °C/min for 1 h under an N_2 atmosphere.

Characterization of biochar

The SBC400, SBC500, SBC600, SBC700, Sar-KOH, and SBC400-KOH samples were characterized by various methods as follows.

The morphological structures of the samples were photographed via field emission scanning electron microscopy (FESEM) (JSM-7800F, JEOL, Japan) equipped with energy dispersive X-ray spectroscopy (EDS) apparatus.

The crystalline structure of the biochar was obtained on an X-ray diffractometer (Ultima IV, Rigaku, Japan) using Cu Kα radiation (λ = 0.15418 nm) in a 2θ range of 10°–90° with a scanning speed of 10°/min.

The surface functional groups and chemical bonds on biochar were measured by FTIR (Fourier transform infrared) spectroscopy (TENSOR 37, BRUKER, Germany) spectroscopy in transmittance mode from 4,000 to 400 cm^{-1}. The biochar was mixed with KBr and then pressed into a flake with a diameter of 15 mm before analysis.

The thermogravimetric analysis (TGA) was conducted on a Mettler Toledo TGA/DSC1 analyzer. Around 20 mg of biochar was loaded and heated from 10 to 1,000 °C with a heating rate of 10 °C/min in N_2 (40 mL/min).

X-ray photoelectron spectrometry (XPS) of the biochar was performed by a Thermo Fisher Scientific ESCALAB 250Xi spectrometer, using 284.6 eV as the C 1s photoelectron peak for calibrating the charge. Deconvolution of the XPS peaks was conducted by CASA XPS software.

The Raman spectra were obtained with a Raman spectrometer (LabRAM HR Evolution, Horiba, Japan). The laser's wavelength was 532 nm, and the testing wavenumber range was 500–2,500 cm^{-1}.

The N_2 adsorption–desorption test was conducted on a multistation automated surface area and porosity analyzer (ASAP 2460, Micromeritics, USA). Prior to analysis, the samples were degassed under a vacuum at 200 °C for 8 h. The specific surface area was calculated from the N_2 adsorption data using the Brunauer–Emmett–Teller (BET) method. The pore size distribution was derived from the adsorption isotherm by applying nonlocal density functional theory (NLDFT).

The CO_2 physisorption isotherms at 273 K were measured using a gas adsorption analyzer (ASAP 2020, Micromeritics, USA) with high-purity CO_2 (> 99.999%). Prior to measurement, each sample was degassed under a vacuum at 200 °C for 6 h to remove moisture and guest molecules.

Temperature-programmed desorption (CO_2-TPD) experiments were conducted with a basic dynamic chemisorption analyzer (ChemiSorb 2720, Micromeritics, USA) to characterize the surface basicity of the biochars. Specifically, 100 mg of biochar was degassed in He (30 mL/min) at 200 °C for 20 min. After the mixture had cooled down to 50 °C, a flow of CO_2 (30 mL/min) was fed for 30 min until reaching the adsorption equilibrium. Then the biochar was heated from 50 to 900 °C with a heating rate of 10 °C/min in a He flow (20 mL/min) and the desorbed CO_2 was detected with a thermal conductivity detector (TCD).

CO_2 adsorption experiments

The CO_2 adsorption experiments were conducted using a thermogravimetric instrument (TGA/DSC1, Mettler Toledo, USA). Prior to adsorption, around 15–20 mg of biochar powder was pretreated under a 40 mL/min N_2 flow by heating from 40 to 120 °C at a rate of 100 °C/min, holding for 90 min to ensure complete degassing, and then cooling to 40 °C. The CO_2 adsorption was then performed at 40 °C and 1 bar for 40 min under a 40 mL/min CO_2 flow, followed by desorption in a 40 mL/min N_2 flow while heating from 40 to 120 °C at 100 °C/min. To elucidate the adsorption kinetics, the experimental data were fitted using the pseudo-first-order (PFO) and pseudo-second-order (PSO) kinetic models. The equations and detailed fitting parameters for these models are provided in Supplementary Text 1. Furthermore, the cyclic adsorption stability was investigated over multiple consecutive adsorption–desorption cycles using the same thermogravimetric analyzer. Each cycle consisted of a 40-min CO_2 adsorption step at 40 °C and 1 bar, followed by a 90-min regeneration step under an N_2 purge at 120 °C.

Results and discussion

Textural characterization of biochar

The textural properties of the biochars were characterized by TGA, XRD, FTIR, and Raman spectroscopy. As shown in Fig. 2a, the thermal decomposition of the *S. tenerrimum* precursor and its derived biochars occurred in three stages (dehydration below 200 °C, pyrolysis from 200 to 550 °C, and aromatization above 550 °C) [31–33]. In contrast, all biochars (SBC400–SBC700) exhibited a markedly lower total weight loss than the *S. tenerrimum* precursor, indicating that increased pyrolysis temperature enhances the thermal stability of the biochar's composition. The XRD patterns (Fig. 2b) revealed a broad and diffuse diffraction peak at 2$\theta \approx$ 15°–30° for all samples, corresponding to the (002) plane of disordered graphitic carbon[34]. The unmodified ABCs displayed additional sharp peaks assigned to halite and sylvite[35,36], reflecting the high inorganic ash content of the feedstock. These peaks were drastically diminished or absent in the KOH-modified samples (SBC400-KOH and Sar-KOH). This transformation is attributed to the chemical reactions during KOH activation, where KOH and derived potassium species (e.g., K, K_2O, K_2CO_3) react with, dissolve, or transform the original inorganic salts (e.g., NaCl, KCl), which are subsequently removed during postactivation washing. This purification step is a critical prerequisite, as it contributes to the development of the high surface area and porosity necessary for enhanced CO_2 adsorption performance. The FTIR spectra (Fig. 2c) showed absorption bands at 3,190 cm^{-1} (–OH), ~1,191 cm^{-1} (C–O), ~1,110 cm^{-1} (C–O–C), ~1,410 cm^{-1} (C=O), 2,930 cm^{-1} and 868 cm^{-1} (aliphatic C–H), ~1,585 cm^{-1} (aromatic C=C), and ~3,325 cm^{-1} (–NH_2)[5,37–40]. The intensities of these bands decreased with increasing pyrolysis temperature, indicating devolatilization, aromatization condensation, dehydration, decarboxylation, decarbonylation, and aromatization[41]. Therefore, the higher CO_2 adsorption capacity of SBC400 in Fig. 3a could be partially attributed to its abundant –OH and/or C=O groups, which can interact with CO_2 molecules via hydrogen bonding and dipole–dipole interactions, respectively. Notably, KOH modification (Sar-KOH and SBC400-KOH) enhanced the –OH and C–O signals compared with SBC400, suggesting the incorporation of additional oxygen-containing groups, which increased the surface polarity and density of potential chemisorption sites for CO_2[26,42]. Raman spectra (Fig. 2d) exhibited D and G bands at ~1,346 and ~1,580 cm^{-1}, respectively[28,43]. For the unmodified biochars, as the pyrolysis temperature increased from 400 °C to 700 °C, the Intensity of D-peak/Intensity of G-peak (I_D/I_G) values increased from 0.88 (SBC400) to 1.32 (SBC700), indicating a rise in structural disorder and defect density at higher temperatures. This trend is commonly associated with the conversion of aliphatic structures into amorphous aromatic clusters and the development of a turbostratic carbon arrangement at higher

temperatures, as also reported in previous studies[28]. Notably, KOH-modified samples showed much higher ratios (2.34 for Sar-KOH, 2.52 for SBC400-KOH), indicating that KOH activation etches the carbon framework and generates abundant defects and pores, which is the fundamental mechanism for creating ultra-microporosity[44]. KOH modification could enhance the graded pore size of Sar-KOH and SBC400-KOH to increase the degree of graphitization, which could help increase the capture sites to boost the CO_2 physisorption ability of biochars[45].

Morphological characteristics of biochar

The morphological evolution of the biochars produced under different pyrolysis temperatures and modification methods was investigated by scanning electron microscopy (SEM), as shown in Fig. 4. The SEM images revealed that the unmodified *Sargassum*-derived biochars (SBC400–SBC700, Fig. 4a–d) exhibited an irregular surface topography, characterized by abundant wrinkles and protrusions. However, no well-defined porous structure was observed across the temperature series, which aligns with their characteristically low specific surface areas (SSAs) as determined by the N_2 adsorption–desorption isotherms (Fig. 5a). The absence of a developed pore architecture in these samples provides a direct morphological explanation for their limited CO_2 adsorption capacity[32,33]. In contrast to the unmodified biochars, both KOH-modified samples (SBC400-KOH and Sar-KOH, Fig. 4e, f) exhibited significantly more developed porous structures. In particular, Sar-KOH, which underwent KOH activation prior to pyrolysis, displayed a highly developed, interconnected porous network (Fig. 4f). SEM-EDS mapping confirmed the homogeneous distribution of elements (C, O, N, Mg, Si, and Au) across this porous surface (Fig. 4g). This well-defined porosity results from severe etching of the carbon framework during KOH activation, a process involving a series of redox reactions between potassium-containing species (e.g., K, K_2O, K_2CO_3) and carbon atoms. These reactions generate substantial gaseous products (e.g., CO, CO_2, H_2, H_2O)[46], whose release selectively etches the carbon matrix to create abundant micropores and mesopores[29,47]. This extensive porous architecture is directly responsible for the enhanced CO_2 adsorption capacity of Sar-KOH. Conversely, SBC400-KOH showed a less developed pore structure compared with Sar-KOH, indicating that postpyrolysis activation was less effective in creating a favorable porous architecture.

Pore structure of biochar

The SSA and pore structure of the biochars were further characterized by their N_2 adsorption–desorption isotherms, as shown in Fig. 5a, b, Table 1, and Supplementary Table S1. The unmodified biochars (SBC400–SBC700) exhibited Type II isotherms with H3-type hysteresis loops, suggesting the presence of slit-shaped mesopores and micropores. SBC400 possessed the lowest SSA of only 1.14 m^2/g,

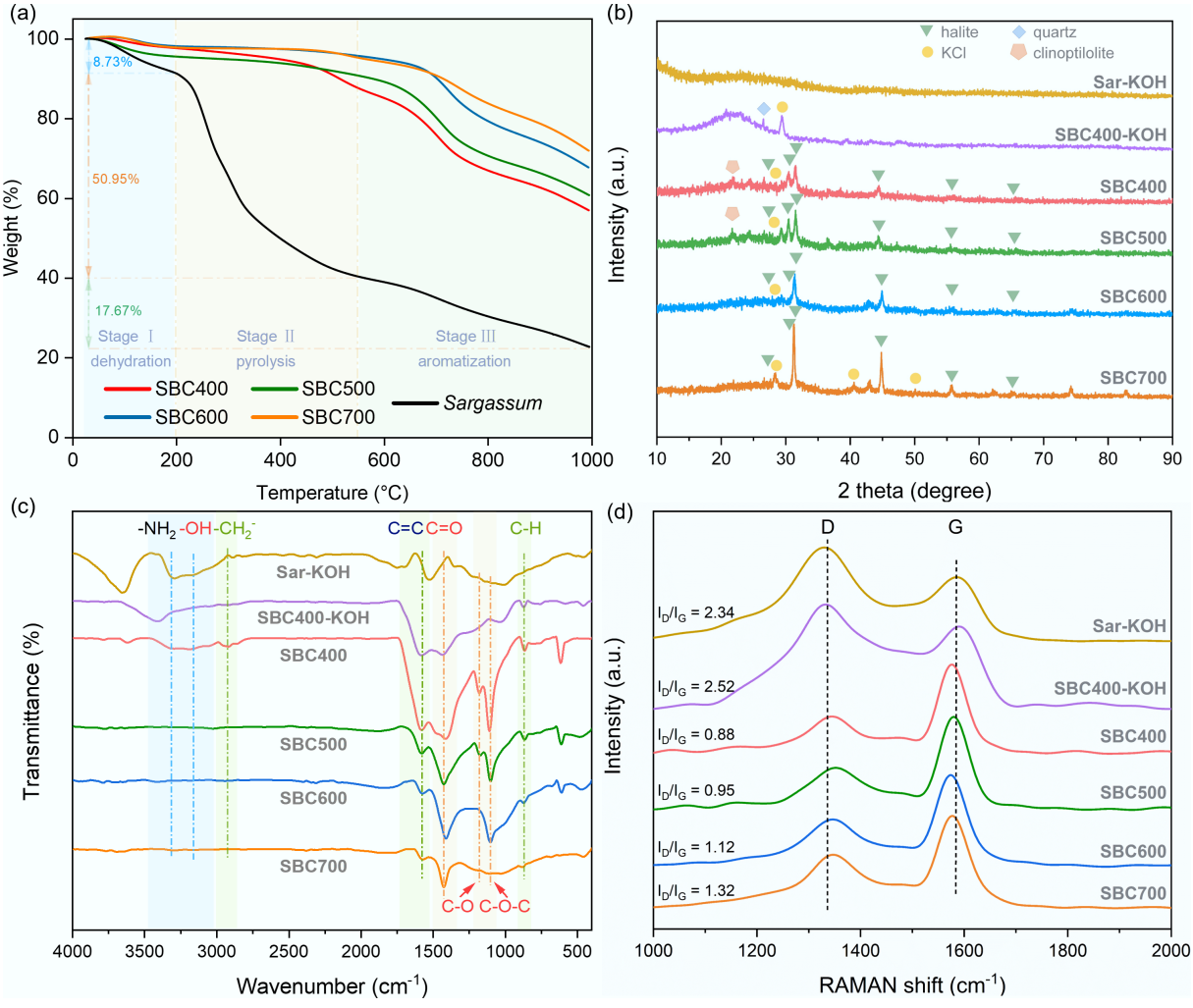

Fig. 2 (**a**) TGA curves of *S. tenerrimum* and its biochars; (**b**) XRD image, (**c**) FTIR pattern, and (**d**) Raman spectra of SBC400, SBC500, SBC600, SBC700, SBC400-KOH, and Sar-KOH.

https://doi.org/10.48130/bchax-0026-0019

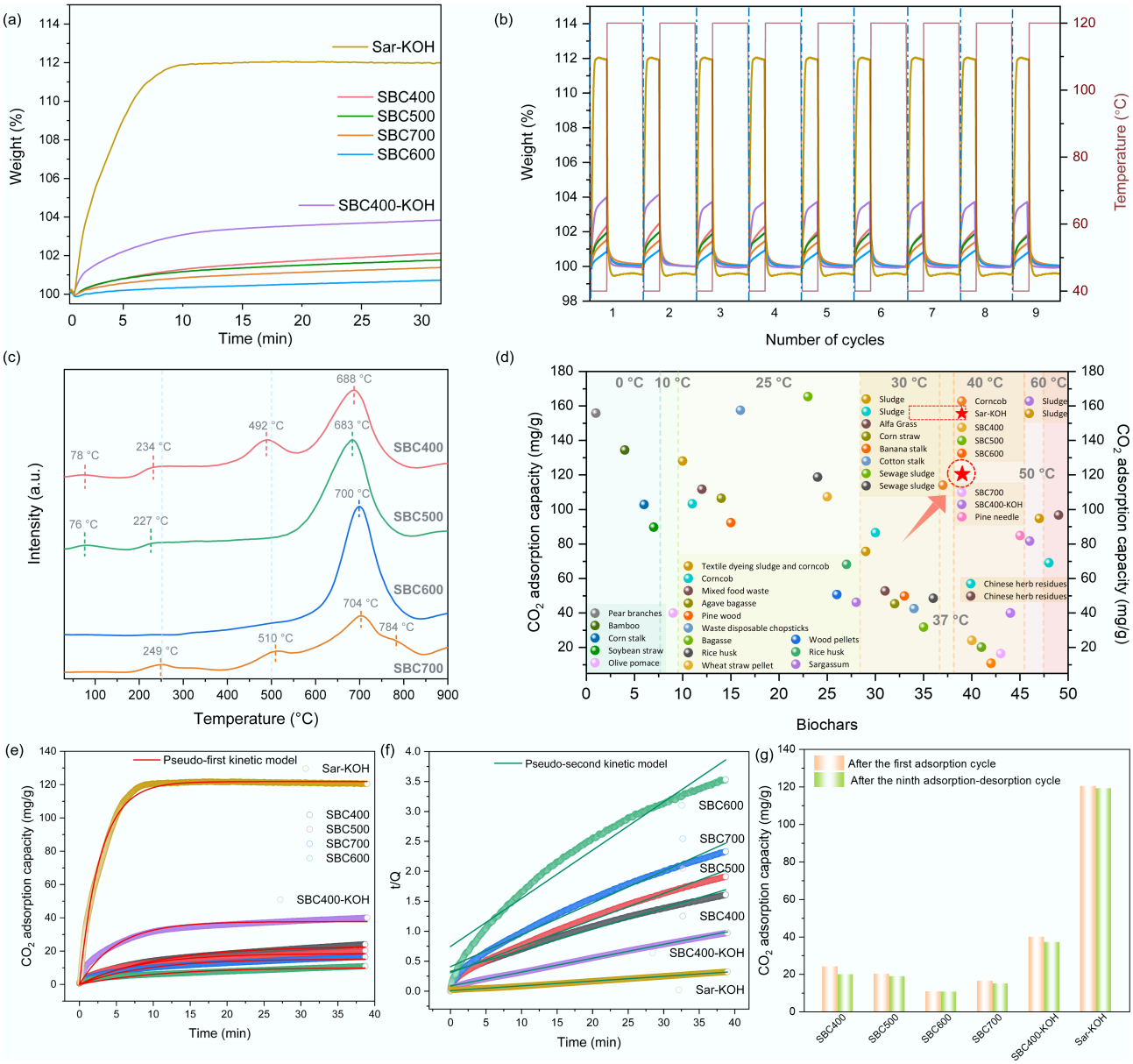

Fig. 3 (**a**) CO_2 adsorption capacity and (**b**) adsorption cycle stability of biochars. (**c**) CO_2-TPD profile of SBC400, SBC500, SBC600, and SBC700. (**d**) Comparison of the CO_2 adsorption capacities of some reported biochars. (**e**) Pseudo-first-order kinetic adsorption curves and (**f**) pseudo-second-order kinetic adsorption curves of biochars for CO_2. (**g**) CO_2 adsorption capacity of biochars after the first adsorption cycle and after the ninth adsorption–desorption cycle.

which is significantly lower than that reported for biochars derived from lignocellulosic biomass[28,48]. This characteristically low SSA of *Sargassum*-derived biochars can be attributed to the high content of hydrophilic polysaccharides and inorganic salts in the feedstock[48]. During pyrolysis, these components promote the formation of tar-like intermediates and facilitate ash melting, which subsequently blocks nascent pores and results in a dense, poorly porous structure, as corroborated by the SEM images (Fig. 4a–d). The low SSA is a primary factor leading to their relatively low CO_2 adsorption capacity. As the pyrolysis temperature increased from 400 to 700 °C, the SSA of the biochars increased from 1.14 m^2/g (SBC400) to 17.11 m^2/g (SBC700). This increase can be attributed to the more complete decomposition of volatiles and the sublimation or transformation of inherent alkali metals (e.g., K, Na) at higher temperatures, which facilitates the creation of additional micropores[49].

KOH activation markedly enhanced the porosity of the biochars. The SSA of SBC400-KOH increased to 9.64 m^2/g. Notably, Sar-KOH achieved a substantially higher SSA of 569.66 m^2/g. This highlights the critical importance of the activation sequence. Prepyrolysis modification enables KOH to interact with the raw biomass during the pyrolysis process, where a series of redox reactions (e.g., $6KOH + 2C \rightarrow 2K + 3H_2 + 2K_2CO_3$) efficiently etches the carbon framework and generate an extensive network of micropores and mesopores[50]. This process produces the highly developed porous morphology observed by SEM (Fig. 4f) and is directly responsible for its high CO_2 adsorption performance. The pore size distribution of Sar-KOH revealed a predominance of micropores. In general, mesopores provide low-resistance pathways for the diffusion of CO_2 molecules, whereas micropores offer numerous adsorption sites and play a more dominant role in CO_2 capture[51].

To accurately evaluate the CO_2 physisorption capacity and micropore structure, CO_2 adsorption–desorption experiments were further conducted on Sar-KOH at 273 K (Fig. 5c). Sar-KOH showed a CO_2 uptake capacity of 558.22 cm^3/g at 273 K. The pore size distribution confirmed its highly microporous nature, with a dominant pore width below 2 nm and a sharp peak at approximately 0.6 nm (Fig. 5d). This well-developed ultra-microporous structure originated from the extensive etching of the carbon framework by KOH during the concurrent activation and carbonization process[28]. It has been established that ultra-micropores with widths below 0.7 nm are particularly effective for CO_2 capture because of the enhanced adsorption potential within these confined spaces[5,27]. Therefore, the abundance of these optimally sized ultra-micropores is the primary reason for the superior CO_2 adsorption capacity of Sar-KOH. In contrast, the lower efficiency of SBC400-KOH, consistent with its less developed pore structure observed by SEM (Fig. 4e), suggests that chemical activation of the precarbonized structure is less effective. This is likely caused by restricted diffusion of the chemical agent into the more ordered and less reactive carbon lattice, resulting in a less favorable porous architecture for adsorption.

CO_2 uptake properties of biochar

CO_2 adsorption capacities

The CO_2 adsorption capacities of the biochars produced at varying pyrolysis temperatures and via different KOH modification methods were evaluated using TGA under ambient pressure. As shown in Fig. 3a, f, and Table 1, the CO_2 uptake of the unmodified biochars exhibited an initial decrease followed by an increase with rising pyrolysis temperature. Specifically, the capacities were 24.1 mg/g for SBC400, 20.2 mg/g for SBC500, 10.9 mg/g for SBC600, and 16.5 mg/g for SBC700. The comparatively higher capacity of SBC400 is primarily attributed to its richer surface basic functional groups, such as –OH, C=O, and $-NH_2$, as identified by FTIR spectroscopy (Fig. 2c). These groups can enhance CO_2 capture via weak chemisorption. The subsequent decrease in CO_2 adsorption from SBC500 to SBC600 correlates with the reduced intensity of these basic functional groups in the FTIR spectra, resulting from their dehydration, decarboxylation, and decarbonylation reactions at elevated temperatures. The observed recovery of adsorption capacity in SBC700, despite the further loss of surface functional groups, can be explained by its significantly increased specific surface area (17.11 m^2/g) and the development of a microporous structure, as confirmed by the N_2 adsorption–desorption isotherms (Fig. 5b, inset). This trend suggests a shift in the dominant adsorption mechanism from a surface chemistry-controlled one to a more porosity-dominated process at higher pyrolysis temperatures.

KOH modification markedly enhanced the CO_2 adsorption performance. The SBC400-KOH sample showed an improved capacity (40.0 mg/g). Notably, the sample premodified with KOH (Sar-KOH) exhibited a higher CO_2 adsorption capacity of 120.5 mg/g. This exceptional performance is attributed to the synergistic effect of

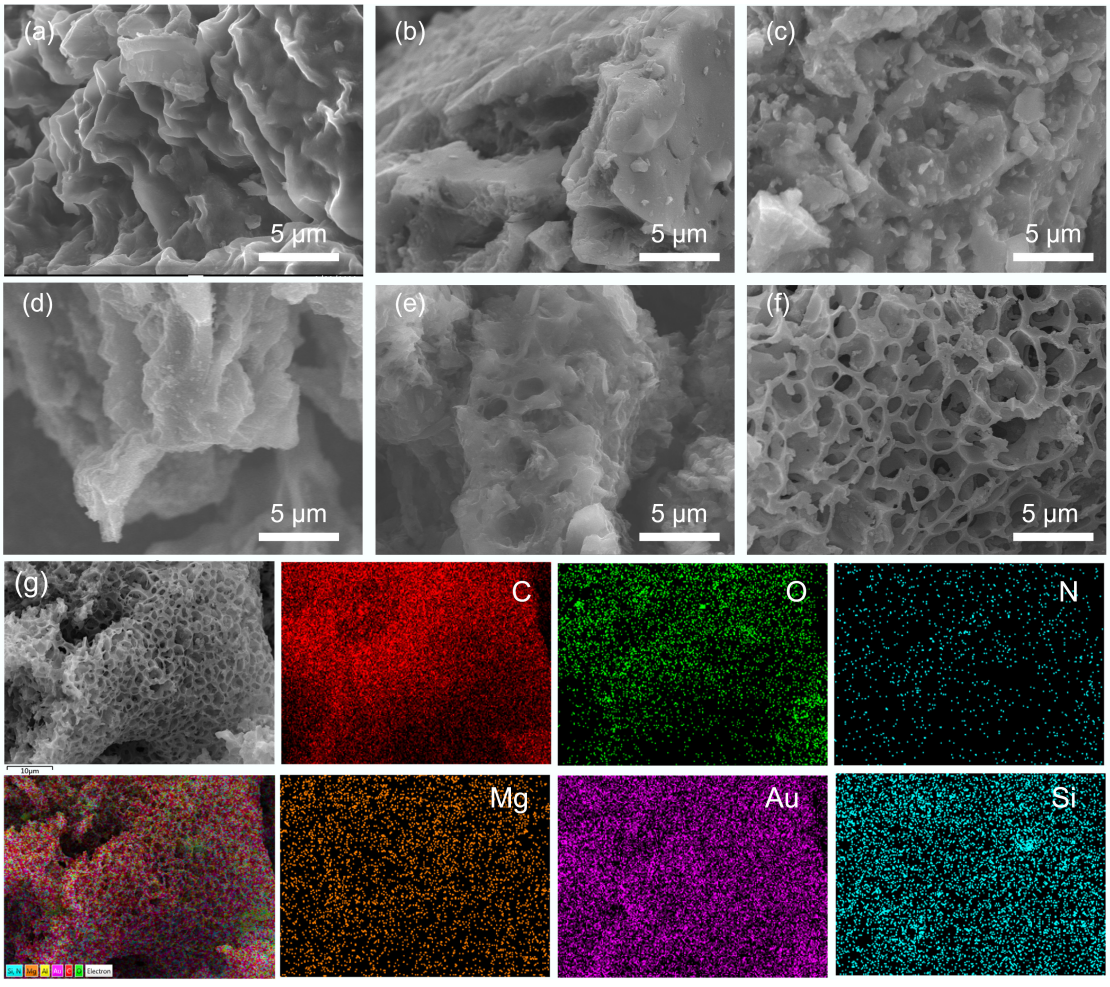

Fig. 4 SEM images of (**a**) SBC400, (**b**) SBC500, (**c**) SBC600, (**d**) SBC700, (**e**) SBC400-KOH, and (**f**) Sar-KOH. (**g**) SEM EDS and elemental mapping images of C, O, N, Mg, Au, and Si in Sar-KOH.

https://doi.org/10.48130/bchax-0026-0019

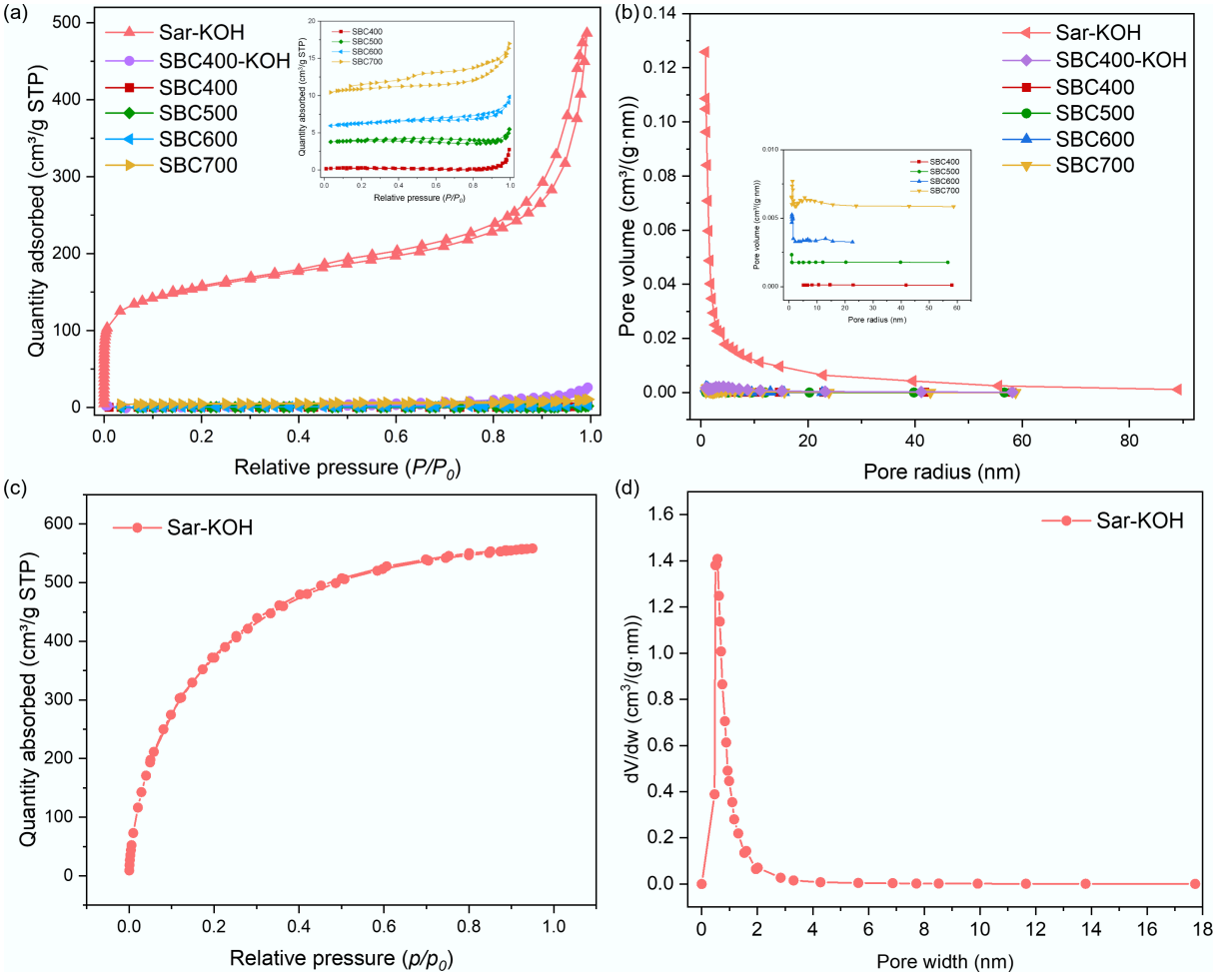

Fig. 5 (**a**) N_2 adsorption–desorption isotherms and (**b**) pore size distributions of SBC400, SBC500, SBC600, SBC700, SBC400-KOH, and Sar-KOH. (**c**) CO_2 adsorption–desorption isotherm at 273 K and (**d**) the pore size distribution of Sar-KOH.

its well-developed microporous structure, as evidenced by the SEM and N_2/CO_2 physisorption results (Figs. 4f, 5), along with the introduction of stable basic surface groups (including –OH and $–NH_2$) during KOH activation, as seen in the FTIR spectra (Fig. 2c). The combination of a high SSA with a dominant ultra-micropore volume (< 0.7 nm) and favorable surface chemistry makes Sar-KOH an efficient adsorbent for CO_2 capture.

Adsorption kinetics

To assess the practical application potential of biochars for CO_2 capture, both high capacity and rapid adsorption kinetics are crucial. The adsorption kinetics were therefore analyzed by fitting the experimental data (Fig. 3a) with the PFO and PSO kinetic models. The PFO model typically describes processes where physical adsorption or diffusion may be rate-limiting, whereas the PSO model is often more applicable when chemisorption (surface reaction) is the rate-determining step[52]. As shown in Fig. 3e, f, and Table 2, the kinetic profiles of the biochars at 40 °C were better described by the PSO model, which consistently yielded a higher R^2 than the PFO model. For the KOH-modified samples (SBC400-KOH and Sar-KOH), the R^2 values for the PSO model exceeded 0.99. This high fit suggests that chemisorption, facilitated by the abundant basic oxygen-containing functional groups introduced via KOH activation, plays a significant role in the CO_2 capture process for these samples. Furthermore, the time required to reach adsorption equilibrium varied considerably among the samples. Sar-KOH achieved equilibrium in around 11 min, followed by SBC400-KOH (~13 min), whereas the unmodified biochars required 26–28 min. Correspondingly, the initial adsorption rates increased from 0.090–0.123 min^{-1} for the unmodified biochars to 0.199 min^{-1} for SBC400-KOH and 0.351 min^{-1} for Sar-KOH. Sar-KOH thus exhibited not only the fastest equilibration time but also the highest adsorption rate, indicating markedly enhanced kinetics. Notably, for Sar-KOH, the R^2 values of both the PFO and PSO models were above 0.99, indicating that the adsorption process is complex and is governed by a combination of concurrent physical and chemical mechanisms.

Table 1 Textural parameter and CO_2 adsorption capacities of the biochars

Sample	SBC400	SBC500	SBC600	SBC700	SBC400-KOH	Sar-KOH
Specific Surface Area determined by the BET method (S_{BET}) (m^2/g)	1.14	1.37	2.61	17.11	9.64	569.66
CO_2 adsorption capacity (mg/g)	24.1	20.2	10.9	16.5	40.0	120.5
Loss of adsorption capacity after 9 cycles (%)	17.0	6.4	2.8	8.5	7.0	1.1

Table 2 Adsorption kinetic parameters of CO_2 on biochar at 40 °C

Sample	Pseudo-first order model			Pseudo-second order model		
	$q_t = q_e(1-e^{-k_1 t})$			$q_t = t \times k_2 \times q_e^2/(1+q_e \times t \times k_2)$		
	q_e (mg/g)	k_1 (1/min)	R^2	q_e (mg/g)	k_2 (g/(mg·min))	R^2
SBC400	22.96	0.095	0.965	28.425	0.004	0.984
SBC500	18.65	0.123	0.940	22.650	0.006	0.989
SBC600	10.18	0.090	0.892	12.427	0.009	0.957
SBC700	15.41	0.111	0.930	18.779	0.007	0.982
SBC400-KOH	37.74	0.199	0.962	43.103	0.006	0.999
Sar-KOH	121.83	0.351	0.994	125.786	0.008	0.997

Comparative performance benchmarking

To contextualize the performance of the optimized adsorbent, the CO_2 adsorption capacity of Sar-KOH was benchmarked against a range of recently reported biochar-based adsorbents, as shown in Fig. 3d and Supplementary Table S2. Since the physisorption of CO_2 onto porous solids is an exothermic process[5], an increase in adsorption temperature typically reduces the equilibrium uptake capacity for most adsorbents within a moderate temperature range (e.g., 0–60 °C). This is primarily caused by the decreased stability of the adsorbed CO_2 molecules at higher thermal energy, which favors desorption. The comparative analysis revealed that Sar-KOH exhibits a relatively higher CO_2 uptake, surpassing a significant number of KOH-activated biochars derived from conventional lignocellulosic biomass. These results position Sar-KOH as a highly promising adsorbent for practical CO_2 capture applications.

Adsorbent regenerability and cyclic stability

The recyclability of CO_2 adsorbents is a critical parameter for assessing their practical application potential. The regeneration stability of the biochars was evaluated by performing multiple adsorption–desorption cycles under alternating CO_2 and N_2 atmospheres using TGA. As shown in Fig. 3b and Table 1, each adsorption–desorption step proceeded rapidly. After nine consecutive cycles, the CO_2 adsorption capacity losses for SBC400, SBC500, SBC600, SBC700, SBC400-KOH, and Sar-KOH were 17.0%, 6.4%, 2.8%, 8.5%, 7.0%, and 1.1%, respectively (Table 1). The minimal capacity loss exhibited by Sar-KOH indicates that the carbon structure formed through prepyrolysis KOH activation possesses superior thermal and mechanical stability. Regeneration under an inert gas atmosphere effectively restored its adsorption capacity without significant structural degradation, which can be attributed to the highly stable microporous architecture created during the simultaneous carbonization and activation processes[53]. Owing to its exceptional cyclic stability, high initial CO_2 adsorption capacity, and rapid kinetics, Sar-KOH emerges as a particularly promising candidate for practical CO_2 capture applications where long-term adsorbent performance is essential for economic viability.

Adsorption mechanisms of biochar

To investigate the chemical interaction between CO_2 molecules and the biochars, CO_2-TPD analysis was performed, as shown in Fig. 3c. Basic sites are typically classified into three types according to the desorption temperature: Desorption peaks below 250 °C are attributed to weakly adsorbed CO_2, those between 250 and 450 °C correspond to moderate-strength basic sites, and peaks above 450 °C generally reflect strong chemisorption[54]. It should be noted that desorption peaks above 450 °C originated from the thermal decomposition of the biochar matrix itself, releasing CO and CO_2[55]. Since CO_2 capture processes are generally conducted at around room temperature, the low temperature desorption region is considered more relevant for assessing practical adsorption performance. It can be seen that SBC400 and SBC500 exhibited two low-temperature desorption peaks at 76–78 and 227–232 °C. These peaks can be ascribed to weak basic sites, such as –OH and $–NH_2$ groups, which interact with CO_2 via hydrogen bonding and weak acid–base interactions, respectively[5]. The presence of these functional groups, which was also confirmed by the FTIR results (Fig. 2c), contributes to the relatively higher CO_2 adsorption capacities of SBC400 and SBC500. As the pyrolysis temperature increased from 400 to 700 °C, the intensity of these functional groups progressively diminished, consistent with the FTIR observations, resulting in reduced contributions from the weak basic sites to CO_2 adsorption. In contrast, SBC700 displayed a desorption peak at 249 °C, which arose from the enhanced physisorption within its developed micropores, as supported by its pore size distribution (Fig. 5b, inset). The marked decline in CO_2 uptake observed for SBC500 and SBC600 can be linked to the loss of weak basic functional groups combined with insufficient development of microporosity. In particular, the low adsorption capacity of SBC600 is caused by the absence of both effective surface functional groups and a well-developed microporous structure. These results highlight that effective CO_2 capture by *Sargassum*-derived biochars depends on the synergistic effect between developed micropores and the presence of weak basic surface functional groups.

XPS analysis was conducted to further elucidate the surface chemical states and elemental composition of the biochars (Fig. 6 and Supplementary Table S3). The survey spectra (Fig. 6a) exhibited two dominant peaks corresponding to C 1s (~284 eV) and O 1s (~531 eV). To identify and quantify the specific chemical functionalities, the high-resolution spectra of C, O, and N were deconvoluted, as shown in Fig. 6b–e and Supplementary Table S4. High-resolution deconvolution of the C 1s spectrum (Fig. 6b) was fitted with five component peaks located at 284.8, 286.3, 286.9, 288.2, and 288.8 eV, corresponding to C–C, C–N, C–O, C=O, and O–C=O bonds, respectively[28]. The O 1s spectrum (Fig. 6c) was resolved into two peaks at 531.7 and 533.5 eV, attributed to O–H and C–O groups[56]. Quantitative analysis of the oxygen functional groups (Fig. 6d) revealed that Sar-KOH possesses the highest relative content of O–H, which aligns with the FTIR observations (Fig. 2c). This prominent population of hydroxyl groups supports their role in enhancing CO_2 adsorption through dipole–dipole interactions and hydrogen bonding[57]. Furthermore, the N 1s spectra indicated the presence of two N dopant species, including pyridinic N (398.6 eV) and pyrrolic N (400.2 eV) (Fig. 6e)[58]. It can be seen that KOH modification induced a general decrease in the total nitrogen content of the biochars. Pyridinic N became the dominant nitrogen species in SBC600, suggesting a transformation in the nitrogen bonding configuration at higher pyrolysis temperatures. These findings demonstrate that the prepyrolysis KOH activation (Sar-KOH) creates an oxygen-rich surface dominated by hydroxyl groups, which synergizes with its developed porosity to achieve superior CO_2 adsorption. In contrast, the thermal evolution and loss of nitrogen species

https://doi.org/10.48130/bchax-0026-0019

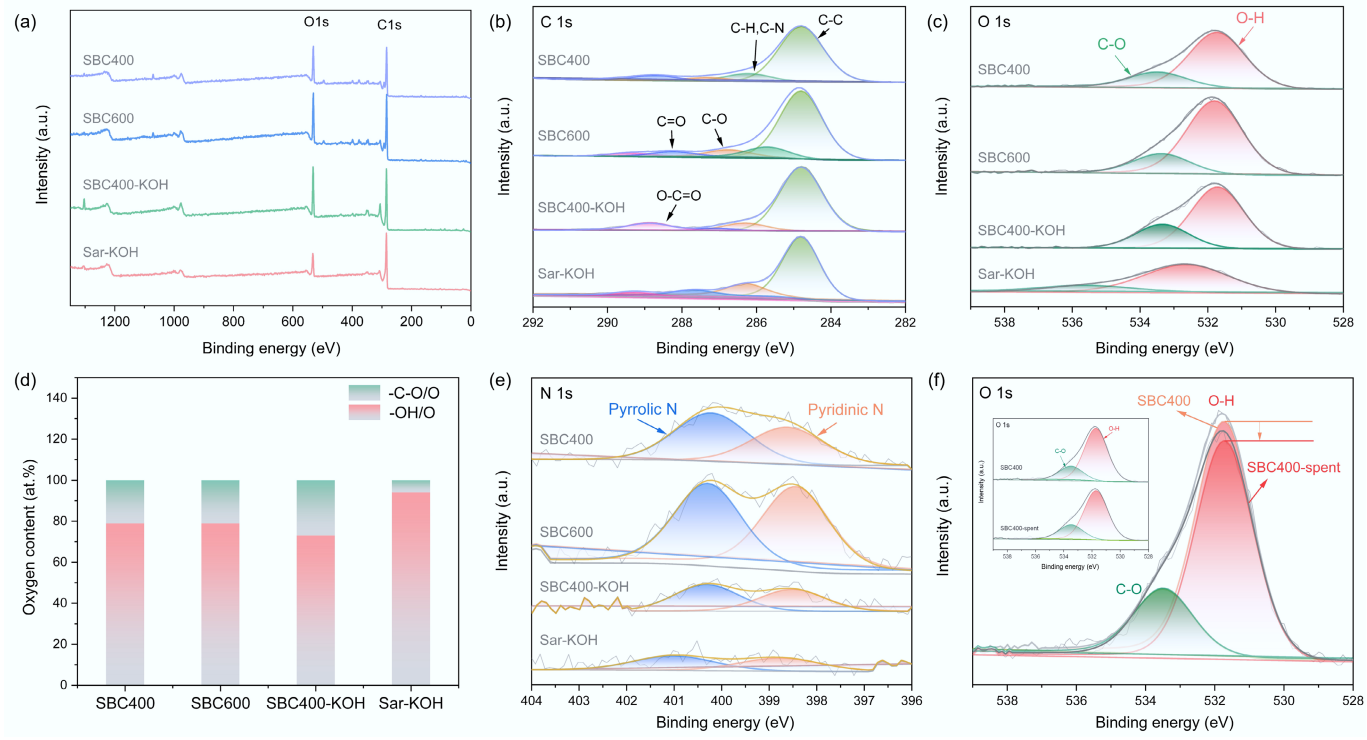

Fig. 6 (**a**) XPS survey spectra and typical (**b**) C 1s, (**c**) O 1s spectra. (**d**) Relative content of –C–O and –OH groups. (**e**) N 1s spectra of SBC400, SBC600, SBC400-KOH, and Sar-KOH and (**f**) O 1s spectra of SBC400 before and after CO_2 adsorption.

across the temperature series highlight the thermal restructuring of the carbon matrix[59]. Integrating these chemical insights with the structural data from the BET and SEM analyses establishes that the high performance of Sar-KOH arises from the optimal integration of a microporous framework with a polar, oxygen-functionalized surface.

To gain a deeper insight into the evolution of electronic behavior during CO_2 adsorption, a comparative XPS analysis was conducted on biochar before and after CO_2 capture. SBC400 was selected because of its low SSA, which minimizes the interference of physisorption and allows for a clearer investigation of the chemical interactions. The sample after CO_2 adsorption was named SBC400-spent. The evolution of surface chemical states and the redistribution of electron density of SBC400 and SBC400-spent, including their characteristic binding energy shifts and changes in peak intensities, is shown in Fig. 6f. It can be seen that the relative content of the O–H species in SBC400-spent decreased after CO_2 capture, which suggests the involvement of surface hydroxyl groups in the adsorption process[60]. This result provides direct surface chemical evidence supporting the existence of the weak basic sites (O–H groups) identified in the CO_2-TPD analysis and FTIR results, confirming their active role in the chemisorption of CO_2.

In summary, the superior CO_2 capture performance of Sar-KOH arises from a synergistic interplay between its well-developed ultra-micropores and abundant surface hydroxyl groups. The ultra-micropores (predominantly < 0.7 nm) provide a confined space that enhances physisorption via overlapping adsorption potentials, whereas the hydroxyl groups act as weak basic sites that promote chemisorption through hydrogen bonding with CO_2 molecules. This adsorption mechanism enables Sar-KOH to achieve both high capacity and fast kinetics. The combination of an optimized pore architecture and tailored surface chemistry, achieved by prepyrolysis KOH activation at a moderate temperature (400 °C) thus represents an effective strategy for designing high-performance algal biochar adsorbents.

Lifecycle assessment of CO_2 capture by Sar-KOH

A preliminary life cycle assessment (LCA) was conducted to evaluate the environmental performance of a CO_2 capture system utilizing the optimized biochar adsorbent, Sar-KOH, with a focus on global warming potential (GWP) and energy demand. The assessment followed a 'cradle-to-regeneration' approach. The system boundaries encompassed the collection and transportation of *S. tenerrimum* biomass, production of the biochar via pyrolysis and KOH activation at 400 °C, the CO_2 adsorption phase, and 18 consecutive adsorption–desorption regeneration cycles of the spent adsorbent. The functional unit was defined as the capture and sequestration of 1 kg of CO_2 by Sar-KOH. According to the experimental adsorption data (Supplementary Table S5), capturing 1 kg of CO_2 requires approximately 0.47 kg of Sar-KOH, accounting for its stable capacity over 18 cycles. With a biochar yield of 50 wt.% at 400 °C (determined by TGA, Fig. 2a), this corresponds to a feedstock requirement of about 0.94 kg of dry *S. tenerrimum*. Key inventory data, including the specific energy demand for pyrolysis (2.8 MJ/kg biomass) and regeneration (0.2 MJ/kg CO_2 per cycle), were sourced from the literature and are summarized in Table 3[61].

The lifecycle inventory analysis yielded the following aspects of primary energy consumption: (i) Pyrolysis and activation energy, 0.94 kg feedstock × 2.8 MJ/kg = 2.63 MJ; (ii) regeneration energy (18 cycles): 18 × 0.2 MJ/kg CO_2 = 3.6 MJ; (iii) transportation energy: negligible (~0.009 MJ). The total energy demand was thus calculated to be approximately 6.24 MJ. Using an average grid electricity emission factor of 0.41 kg CO_2-eq/kWh[62], the indirect greenhouse gas emissions associated with this energy equal (6.24 MJ / 3.6 MJ/kWh) × 0.41 kg CO_2-eq/kWh ≈ 0.71 kg CO_2-eq. Therefore, the net CO_2 removal achieved by the proposed system is: 1.00 kg (captured) – 0.71 kg (embodied emissions) = 0.29 kg CO_2-eq per kg

Table 3 Lifecycle inventory

Process	Parameter	Value
Feedstock	Carbon content in biochar Biochar yield from *Sargassum tenerrimum* pyrolysis	~50% (mass basis) ~50% by mass
Pyrolysis and activation[61]	Thermal demand at 400 °C	~2.8 MJ/kg biomass
Regeneration[61]	Energy for CO_2 desorption	~0.2 MJ/kg CO_2
Transport	Biomass delivery (truck, 50 km)	~0.1 MJ/ton km
Energy mix[62]	Grid emission factor (Qinghai, China)	0.41 kg CO_2-eq/kwh

of CO_2 captured. This positive net balance indicates that the Sar-KOH-based system achieves net negative emissions, providing a net climate benefit. The result highlights the promising CO_2 removal potential of the material at the laboratory scale. When integrated with the previously demonstrated high adsorption capacity, rapid kinetics, and excellent cyclic stability, these LCA findings support the technical and environmental rationale for the further development and potential scalability of the proposed direct air capture system, positioning it as a viable candidate for climate change mitigation strategies.

Limitations and future research directions

Despite the promising CO_2 capture performance of Sar-KOH demonstrated in this study, several limitations should be acknowledged. First, all the adsorption experiments were conducted under dry conditions, whereas real flue gas or air contains moisture. The presence of moisture may affect the CO_2 adsorption capacity, CO_2's selectivity over other gases (e.g., N_2, O_2), and the stability of the biochar adsorbent through competitive adsorption or potential hydrolysis of the surface functional groups. Therefore, systematic investigation of the influence of relative humidity on the adsorption performance of Sar-KOH is a prerequisite for practical applications. Second, the adsorbent was used as a powder, which may cause a high pressure drop in fixed-bed reactors. Future work should explore processing Sar-KOH into mechanically robust particles, pellets, or monolithic structures using appropriate binders and shaping techniques, followed by an evaluation of their pressure drop characteristics, mechanical strength, and cyclic stability under dynamic flow conditions. Third, further modification strategies such as nitrogen doping could be explored to enhance the surface's basicity and CO_2 affinity. Addressing these limitations will facilitate the translation of Sar-KOH to practical carbon capture technologies.

Conclusions

In this study, a promising *Sargassum*-derived biochar pyrolyzed at 400 °C and modified with KOH was reported to have abundant micropores and hydroxyl groups. Its potential use as a CO_2 adsorbent was demonstrated by its high CO_2 adsorption capacity and stable regeneration performance. Comprehensive characterizations confirm that this superior performance originates from a synergistic effect: The prepyrolysis KOH activation at a moderate temperature serves as the critical step, simultaneously creating an ultra-microporous architecture via severe etching of the carbon framework and enriching the surface with hydroxyl groups. The developed micropores provide abundant physisorption sites for CO_2 molecules, whereas the hydroxyl groups enhance the surface's basicity and facilitate specific interactions (hydrogen bonding) with CO_2 molecules. In summary, the strategic integration of controlled pyrolysis temperature and preactivation offers an effective pathway to design algae-derived biochar with an optimized porosity and surface chemistry for efficient CO_2 capture. This approach not only advances adsorbent design but also promotes the valorization of algal biomass, addressing both environmental and resource challenges.

Supplementary information

It accompanies this paper at https://doi.org/10.48130/bchax-0026-0019.

Ethical statements

This work represents the authors' own intellectual contribution, and no AI tools have been used.

Author contributions

The authors confirm their contributions to the paper as follows. Yuanling Li: conceptualization, methodology, data analysis, writing – original draft preparation; Tao Wang: methodology, experiments, and data analysis; Jinyu Zhu: experiments; Siyu Duan: experiments; Lina Liu: conceptualization, methodology, review and editing, supervision, funding acquisition. All authors have read and agreed to the published version of the manuscript.

Data availability

The datasets generated during and/or analyzed during the current study are available from the corresponding author on reasonable request.

Funding

The authors gratefully acknowledge financial support by the National Natural Science Foundation of China (U24A20519, 22376109), the Shanxi Provincial Foundation Research Program (Project No. 202403021212054), the Taiyuan University of Science and Technology Scientific Research Initial Funding (Project No. 20232105), the Reward for Doctoral Work in Shanxi (Project No. 20242042), the Taiyuan University of Science and Technology Innovation and Entrepreneurship Training Program for students (Project No. DCX2025119), and the Key Technology Development for Functional Materials with Efficient Synergistic Adsorption of Heavy Metals and Antibiotics (Project No. 2025505).

Declarations

Competing of interest

The authors declare that they have no conflict of interest.

Author details

[1]School of Environment and Resources, Taiyuan University of Science and Technology, Taiyuan 030024, China; [2]College of Environmental Science and Engineering, Nankai University, Tianjin 300350, China; [3]School of Environment and Energy, Peking University, Shenzhen Graduate School, Shenzhen 518055, China

References

[1] Mapstone G, Kamsma TM, Xu Z, Jones PK, Lee AA, et al. 2025. Understanding the mechanism of electrochemical CO_2 capture by supercapacitive swing adsorption. *ACS Nano* 19:4242–4250

[2] Pye S, Li FGN, Price J, Fais B. 2017. Erratum: Achieving net-zero emissions through the reframing of UK national targets in the post-Paris Agreement era. *Nature Energy* 2:17088

[3] Xie Z, Cheng W, Luo H, Lei Y, Shi W. 2026. Artificial photothermal synthesis of hydrocarbons from CO_2 and H_2O. *Advanced Energy Materials* 16:2501840

[4] Hussain B, Batool K, Ali Naqvi SA, Nassani AA, Ali S. 2025. Racing towards environmental sustainability by lowering fossil resources in the energy mix during era of global boiling. *Applied Energy* 390:124847

[5] Li Y, Liu L, Yu H, Zhao Y, Dai J, et al. 2022. Synergy of developed micropores and electronic structure defects in carbon-doped boron nitride for CO_2 capture. *Science of the Total Environment* 811:151384

[6] Jiao X, Lin J, Zhang R, Deng T, Yu C, et al. 2025. Constructing of porous boron nitride granules for dynamic adsorption of CO_2. *Separation and Purification Technology* 362:131727

[7] Zhang R, Cui G, Wang X, Chen Y, Qiu X, et al. 2024. Ionic liquid-based advanced porous organic hyper-crosslinked polymers (ILHCPs) for CO_2 capture and conversion. *Chemical Engineering Journal* 489:151102

[8] Aizaz U, Ul Hassan I, Onaizi SA. 2025. MXenes-based materials for CO_2 capture and conversion: a comprehensive review. *Renewable and Sustainable Energy Reviews* 214:115524

[9] He Y, Boone P, Lieber AR, Tong Z, Das P, et al. 2023. Implementation of a core-shell design approach for constructing MOFs for CO_2 Capture. *ACS Applied Materials & Interfaces* 15:23337−23342

[10] Guan J, Dai Z, Zhou H, Huang Z, Wang X, et al. 2025. Design, synthesis, and screening of COFs for CO_2 adsorption by gaussian process. *ACS Applied Materials & Interfaces* 17:58628−58638

[11] Di H, Zhang T, Ma H, Zhang G, Li K, et al. 2025. Biomass tar modified biochar with enhanced micropores and oxygen content for high efficiency CO_2 capture. *Separation and Purification Technology* 378:134678

[12] Zhang G, Ren R, Yan X, Zhu Y, Zhang H, et al. 2025. The key role of magnetic iron-to-biochar mass ratios in the dissipation of oxytetracycline and its resistance genes in soils with and without biodegradable microplastics. *Journal of Environmental Management* 377:124658

[13] Zhang T, Jiku MAS, Li L, Ren Y, Li L, et al. 2023. Soil ridging combined with biochar or calcium-magnesium-phosphorus fertilizer application: enhanced interaction with Ca, Fe and Mn in new soil habitat reduces uptake of As and Cd in rice. *Environmental Pollution* 332:121968

[14] Zhang F, Zhang G, Liao X. 2021. Negative role of biochars in the dissipation and vegetable uptake of polycyclic aromatic hydrocarbons (PAHs) in an agricultural soil: cautions for application of biochars to remediate PAHs-contaminated soil. *Ecotoxicology and Environmental Safety* 213:112075

[15] Feng G, Tian Z, Wang J. 2023. Effects of rice husk powder and thermal hydrolysis on sludge characteristics. *Water Science & Technology* 87:2315−2327

[16] Li Y, Yu H, Liu L, Yu H. 2021. Application of co-pyrolysis biochar for the adsorption and immobilization of heavy metals in contaminated environmental substrates. *Journal of Hazardous Materials* 420:126655

[17] Shafawi AN, Mohamed AR, Lahijani P, Mohammadi M. 2021. Recent advances in developing engineered biochar for CO_2 capture: an insight into the biochar modification approaches. *Journal of Environmental Chemical Engineering* 9:106869

[18] Luo S, Liu Z, Yin X, Zhang S, Guo M. 2026. Ag/$CoFe_2O_4$@Biochar for interfacial solar steam generation and heavy metal removal. *Advanced Functional Materials* 36:e16492

[19] Li Z, Chen K, Zhai S, Yang L, Yu T, et al. 2024. Preparation of biochar from anaerobic digested sludge for enhancement of sludge dewatering. *Chemosphere* 362:142687

[20] Nguyen TB, Do QH, Doong RA, Chen WH, Chen CW, et al. 2025. Phosphorized ZIF-67 on cow manure biochar for sulfite-activated degradation of bisphenol S in aqueous solution. *Chemical Engineering Journal* 521:167080

[21] Li T, Zhu F, Liang W, Hu G, Deng X, et al. 2022. Simultaneous removal of p-nitrophenol and Cr(VI) using biochar supported green synthetic nano zero valent iron-copper: mechanistic insights and toxicity evaluation. *Process Safety and Environmental Protection* 167:629−640

[22] Sikiru S, Abioye KJ, Adedayo HB, Adebukola SY, Soleimani H, et al. 2024. Technology projection in biofuel production using agricultural waste materials as a source of energy sustainability: a comprehensive review. *Renewable and Sustainable Energy Reviews* 200:114535

[23] Ji L, Ge Q, Li Y, Gao Y, Xie S. 2021. A comparative study of the growth and nutrient removal effects of five green microalgae in simulated domestic sewage. *Water* 13:3613

[24] Li Y, Fang L, Cao G, Mi W, Lei C, et al. 2024. Reservoir regulation-induced variations in water level impacts cyanobacterial bloom by the changing physiochemical conditions. *Water Research* 59:121836

[25] Dissanayake PD, You S, Igalavithana AD, Xia Y, Bhatnagar A, et al. 2020. Biochar-based adsorbents for carbon dioxide capture: a critical review. *Renewable and Sustainable Energy Reviews* 119:109582

[26] Lü F, Lu X, Li S, Zhang H, Shao L, et al. 2022. Dozens-fold improvement of biochar redox properties by KOH activation. *Chemical Engineering Journal* 429:132203

[27] Ge C, Song J, Qin Z, Wang J, Fan W. 2016. Polyurethane foam-based ultramicroporous carbons for CO_2 capture. *ACS Applied Materials & Interfaces* 8:18849−18859

[28] Zhang T, Sun L, Sun X, Dong H, Yu H, et al. 2022. Radical and non-radical cooperative degradation in metal-free electro-Fenton based on nitrogen self-doped biochar. *Journal of Hazardous Materials* 435:129063

[29] Chen W, Gong M, Li K, Xia M, Chen Z, et al. 2020. Insight into KOH activation mechanism during biomass pyrolysis: chemical reactions between O-containing groups and KOH. *Applied Energy* 278:115730

[30] Deng L, Zhao Y, Sun S, Feng D, Zhang W. 2024. Preparation of corn straw-based carbon by 'carbonization-KOH activation' two-step method: gas–solid product characteristics, activation mechanism and hydrogen storage potential. *Fuel* 358:130134

[31] Biswas B, Singh R, Krishna BB, Kumar J, Bhaskar T. 2017. Pyrolysis of azolla, sargassum tenerrimum and water hyacinth for production of bio-oil. *Bioresource Technology* 242:139−145

[32] Kim SS, Ly HV, Kim J, Choi JH, Woo HC. 2013. Thermogravimetric characteristics and pyrolysis kinetics of alga *Sagarssum* sp. biomass. *Bioresource Technology* 139:242−248

[33] Yao B, Chao L, Zhang Y, Liu Y, Zhou C, et al. 2025. Microwave-assisted pyrolysis of spent bleaching clay: a study of pyrolysis characteristics, kinetics, and intrinsic mechanism. *Chemical Engineering Journal* 513:162613

[34] Li R, Huang H, Wang JJ, Liang W, Gao P, et al. 2019. Conversion of Cu(II)-polluted biomass into an environmentally benign Cu nanoparticles-embedded biochar composite and its potential use on cyanobacteria inhibition. *Journal of Cleaner Production* 216:25−32

[35] Kyriakou M, Chatziiona VK, Costa CN, Kallis M, Koutsokeras L, et al. 2019. Biowaste-based biochar: a new strategy for fermentative bioethanol overproduction via whole-cell immobilization. *Applied Energy* 242:480−491

[36] Yu C, Wang M, Dong X, Shi Z, Zhang X, et al. 2017. Removal of Cu(ii) from aqueous solution using Fe_3O_4–alginate modified biochar microspheres. *RSC Advances* 7:53135−53144

[37] Poo KM, Son EB, Chang JS, Ren X, Choi YJ, et al. 2018. Biochars derived from wasted marine macro-algae (*Saccharina japonica* and *Sargassum fusiforme*) and their potential for heavy metal removal in aqueous solution. *Journal of Environmental Management* 206:364−372

[38] Naga Babu A, Srinivasa Reddy D, Krishna Mohan GV, Suresh Kumar G, Dora TK. 2023. Mathematical investigation into the sequential adsorption of silver ions and brilliant green dye using biochar derived from *Gracilaria* Rhodophyta algae. *Biomass Conversion and Biorefinery* 13:10065−10084

[39] Jia X, Zhao X, Zhou Y, Li F, Liu W, et al. 2023. Tri-functional lanthanum-based biochar for efficient phosphorus recovery, bacterial inhibition, and soil fertility enhancement. *Biochar* 5:16

[40] Jia X, Yin T, Li N, Zhang H, Shi A, et al. 2025. Reticulated lanthanum (La) carbonate-carbon composite for efficient phosphorus removal from eutrophic wastewater. *Chinese Chemical Letters* 36:110398

[41] Shafawi AN, Lahijani P, Mohammadi M, Mohamed AR. 2024. An investigation on sequential ultrasonication and metal modification of biochar on its CO_2 capture performance. *Biomass Conversion and Biorefinery* 14:28571−28587

[42] Cui S, Zhao Y, Liu Y, Huang R, Pan J. 2021. Preparation of straw porous biochars by microwave-assisted KOH activation for removal of gaseous H_2S. *Energy & Fuels* 35:18592−18603

[43] Truong QM, Ho PNT, Nguyen TB, Chen WH, Bui XT, et al. 2022. Magnetic biochar derived from macroalgal *Sargassum hemiphyllum* for highly efficient adsorption of Cu(II): influencing factors and reusability. *Bioresource Technology* 361:127732

[44] Xu Q, Jin Y, Zheng F, Lu J. 2023. Exploitation of pomelo peel developing porous biochar by N, P co-doping and KOH activation for efficient CO_2 adsorption. *Separation and Purification Technology* 324:124595

[45] Luo J, Chen Y, Huang H, Ma R, Ma N, et al. 2023. Microwave-coordinated KOH directionally modulated N/O co-doped porous biochar from Enteromorpha and its structure–effect relationships in efficient CO_2 capture. *Chemical Engineering Journal* 473:145279

[46] Su X, Wang X, Ge Z, Bao Z, Lin L, et al. 2024. KOH-activated biochar and chitosan composites for efficient adsorption of industrial dye pollutants. *Chemical Engineering Journal* 486:150387

[47] Jia X, Zhang Y, He Z, Chang F, Zhang H, et al. 2021. Mesopore-rich badam-shell biochar for efficient adsorption of Cr(VI) from aqueous solution. *Journal of Environmental Chemical Engineering* 9:105634

[48] Farobie O, Amrullah A, Bayu A, Syaftika N, Anis LA, et al. 2022. In-depth study of bio-oil and biochar production from macroalgae *Sargassum* sp. via slow pyrolysis. *RSC Advances* 12:9567–9578

[49] Shrivastava P, Kumar A, Tekasakul P, Lam SS, Palamanit A. 2021. Comparative investigation of yield and quality of bio-oil and biochar from pyrolysis of woody and non-woody biomasses. *Energies* 14:1092

[50] Sun M, Ma Y, Yang Y, Zhu X. 2023. Effect of iron impregnation ratio on the properties and adsorption of KOH activated biochar for removal of tetracycline and heavy metals. *Bioresource Technology* 380:129081

[51] Yan Z, Liu Q, Liang L, Ouyang J. 2021. Surface hydroxyls mediated CO_2 methanation at ambient pressure over attapulgite-loaded Ni-TiO_2 composite catalysts with high activity and reuse ability. *Journal of CO_2 Utilization* 47:101489

[52] Zhang X, Xu H, Xiang W, You X, Dai H, et al. 2024. Lignin-impregnated biochar assisted with microwave irradiation for CO_2 capture: adsorption performance and mechanism. *Biochar* 6:22

[53] Li Z, Feng S, Yang X, Lyu H, Wei S, et al. 2025. A review of biomass porous carbon for carbon dioxide adsorption from flue gas: physicochemical properties and performance. *Fuel* 387:134318

[54] Liu L, Dai J, Yang Z, Li Y, Su X, et al. 2022. Plasma-catalytic carbon dioxide conversion by reverse water–gas shift over $La_{0.9}Ce_{0.1}B_{0.5}B'_{0.5}O_{3-\delta}$ perovskite-derived bimetallic catalysts. *Chemical Engineering Journal* 431:134009

[55] Wang X, Yang M, Zhu X, Zhu L, Wang S. 2020. Experimental study and life cycle assessment of CO_2 methanation over biochar supported catalysts. *Applied Energy* 280:115919

[56] Wang HY, Kumar A, Li J, Chen P, Yu ZG, et al. 2023. The adsorption behavior and mechanism for arsenate by lanthanum-loaded biochar with different modification methods. *Environmental Technology & Innovation* 32:103344

[57] Fan K, Wang Y, Tian C, Guan X, Luo X, et al. 2025. Metal-organic frameworks for CO_2 capture: tailoring structure and function through modification strategies. *Chemical Engineering Journal* 522:167344

[58] Guan C, Zhang N, Xie Z, Zheng J, Xia J, et al. 2025. Targeted activation of peroxydisulfate by N/S co-doped nZVI-encapsulated sludge-derived biochar for enrofloxacin degradation: synergistic effect of heterojunctions and active sites. *Separation and Purification Technology* 378:134758

[59] Chen X, Zhu Z, Wang Y, Tao X, Shi X, et al. 2025. Mechanisms of simultaneous activation-ammoniation in co-pyrolysis of cellulose and lignin: synergistic effects on product distribution and characteristics. *Industrial Crops and Products* 237:122285

[60] Jia X, Yin T, Wang Y, Zhou S, Zhao X, et al. 2023. Porous honeycomb cork biochar for efficient and highly selective removal of phosphorus from wastewater. *Biochar* 5:84

[61] Monteagudo JM, Durán A, Zhao Y, Monteagudo J. 2026. CO_2 capture by olive pomace biochar: effect of relative humidity, isosteric heat of adsorption, and a preliminary Life Cycle Assessment investigation. *Separation and Purification Technology* 385:136445

[62] Zhang Y, Zhang Q, Li Y, Gu Y, Wang J, et al. 2025. Mitigation drivers of China's electricity grid revealed by monthly variability of carbon emission factors. *Environmental Science & Technology* 59:25225–25236